Available online at www.sciencedirect.com
ScienceDirect
Journal of Nuclear Materials 373 (2008) 142–149
journal of nuclear materials
www.elsevier.com/locate/jnucmat

Evolution of mechanical properties of SiC under helium implantation

C. Tromas, V. Audurier, S. Leclerc, M.F. Beaufort, A. Declémy, J.F. Barbot *

Laboratoire de Métallurgie Physique UMR6630, Université de Poitiers, SP2MI, Bd M. et P. Curie, BP30179, F-86960 Futuroscope-Chasseneuil cedex, France

Received 13 February 2007; accepted 23 May 2007

Abstract

Mechanical property changes of 4H–SiC implanted at room temperature with helium ions at fluences ranging from 7×10^{15} to 1×10^{17} cm^{-2} and at an ion energy of 50 keV were investigated by using nano-indentation tests and subsequent atomic force microscopy investigations. Degradation of the mechanical properties of the near-surface due to helium implantation was analysed and correlated with the microstructure evolution examined through transmission electron microscopy cross-section and X-ray diffraction experiments. Up to 1×10^{16} He^{+} cm^{-2} no significant change in mechanical properties is seen whereas a normal strain profile of few percents is generated all along the ion path. Nevertheless, the as-created implantation damage enhance the dislocation nucleation. At intermediate fluences, when a buried amorphous layer is created, the hardness curve against penetration depth can be divided into three stages showing 'constraining coating' effects. When the entire part of the implanted crystal is amorphous a decrease of about 50% is measured for hardness value.
© 2007 Elsevier B.V. All rights reserved.

PACS: 62.25.+g; 61.72.Ww

1. Introduction

Under irradiation, materials undergo changes in their structure which in turn affect their mechanical, chemical, or physical properties. In particular, materials used in nuclear technology suffer from degradation to neutron irradiation. Silicon carbide (SiC) fiber-reinforced SiC-matrix composites (SiC/SiC composites) are being considered for structural components in future fusion reactor blankets [1–4]. Displacement damage and transmutation products such as helium (He) will be produced in these composites during high energy neutron irradiation. Helium is found to be the largest product in neutron-irradiated SiC and because of its limited diffusivity in SiC may cause significant swelling and/or stress in the material; the helium production being highly dependent on the neutron energy spectrum [1]. Consequently, studies have been carried out on damage accumulation [5,6] and on the changes in mechanical properties of irradiated SiC with neutrons [6–8] and various ions [9,10]. In general both the hardness and the elastic modulus are found to decrease with increasing fluence. After a full amorphization under neutron irradiation of single crystalline 6H–SiC a strong decrease of 45% in hardness and elastic modulus has been reported [6]. The same trend has been observed in CVD SiC [7]. There have been also some studies on the effects of helium on the microstructural and mechanical properties changes of SiC/SiC composites [11–15]. A small decrease of the bend strength [11] and a brittle behaviour [16] were reported after high temperature implantation but a large increase in strength and a decrease in elastic modulus were also observed after neutron irradiation on helium pre-injected SiC grown by chemical vapor deposition [17]. In B-containing SiC, the formation and growth of He bubbles at grain boundaries were studied together with their effects on mechanical properties [18]. Thus, it appears difficult to accurately quantify the changes on mechanical properties of the different structures involved.

The physical properties of SiC make it also a promising material for advanced semiconductor electronic device

* Corresponding author.
E-mail address: jean.francois.barbot@univ-poitiers.fr (J.F. Barbot).

0022-3115/$ - see front matter © 2007 Elsevier B.V. All rights reserved.
doi:10.1016/j.jnucmat.2007.05.037

applications where conventional silicon-based electronics cannot be operative. The fundamental residual implantation damage and its influence on the mechanical properties is necessary to advance in semi-conductor technological applications. The study of helium implantation into SiC takes also part of research on the SiCOI (silicon carbide-on-insulator) thin films by the smart cut process.

In this paper, we report initial findings from an investigation of the mechanical property changes induced by room temperature helium implantation into 4H–SiC single crystal. The effect of helium-implantation on the mechanical properties of SiC is discussed with regard to the microstructure evolution. Additional information on deformation mechanisms have been achieved by the examination of the indent imprint.

2. Materials and experimental procedure

The n-type $(0001)_{Si}$ 4H–SiC single crystals (8° off-axis towards the $[11\bar{2}0]$ direction, 400 μm thick) used in this study were supplied by Cree Research Incorporation. Implantations with 50 keV He^+ ions were done at room temperature with a current density of about 4 μA cm^{-2} in a fluence range from $7{\times}10^{15}$ up to $1{\times}10^{17}$ cm^{-2}. SRIM calculations [19] predict a projected range R_p of 270 nm and a straggling range δR_p of 60 nm; these calculations were done using threshold displacement energies of 35 and 22 eV for Si and C sublattices [20]. The peak helium concentration is ranging from 0.4 to 8 at.% for a deposited energy density from 1×10^{21} to 20×10^{21} keV cm^{-3}. These values are higher than the threshold values for the formation of observable bubbles for implantation at room temperature and subsequent annealing [21].

Nanoindentation experiments were performed at room temperature with a nanohardness tester (NHT) from CSM instrument (Switzerland) equipped with a diamond Berkovich indenter (triangular based pyramid). The real shape of the indenter was calibrated by the classical method consisting in indenting a fused silica sample at different loads. Assuming that value of the silica Young's modulus is 72 GPa, the contact area between the indenter and the surface is determined as a function of the true penetration depth. The following equation [22]:

$$A_c(h_c) = 21.75h_c^2 + 1480h_c - 2489h_c^{1/2} + 6943h_c^{1/4}$$

fits well the experimental curve for true penetration depths as small as 10 nm. The calibrated shape of the indenter has been also confirmed by direct observations of the Berkovich indenter by AFM. In the following, h_m stands for the maximum penetration depth under maximum load and h_p for the residual penetration depth. For each sample, multi cycle experiments were performed (multiple loading/partial unloading with increasing load) to determine the hardness as a function of the maximum penetration depth, h_m. Each experiment was repeated ten times, to provide a mean value for each penetration depth. The unloading curves were analysed by the Woirgard's method [23] to determine the hardness values.

Atomic force microscopy (AFM) observations were performed with a Dimension 3100 microscope from Veeco (US) in tapping mode. The images were analysed with the WSxM software from Nanotech electronica (Spain) [24].

The microstructure of the implanted samples was investigated using a JEOL-200CX operating at 200 kV. X-ray diffraction (XRD) measurements were conducted in the Bragg (reflection) geometry on an automated laboratory-made two circles goniometer with the Cu $K_{\alpha 1}$ radiation ($\lambda = 1.5405$ Å) provided by a 5 kW RIGAKU RU-200 generator. Previous studies have shown that the strain induced by light ions implantations in SiC is strongly localized along the direction perpendicular to the implanted surface [25]. More details of the XRD setup and of the normal strain determination, $(\Delta d/d)_N$, have been given elsewhere [26].

3. Experimental results and discussion

3.1. Changes in the microstructure

Fig. 1 summarizes in the form of a 'phase diagram' the behavior of 4H–SiC under 50 keV helium ions implantation at room temperature. At low fluences, $\phi \leqslant 10^{16}$ cm^{-2}, the implanted SiC is still crystalline (c-SiC) but strained. Fig. 2(a) shows the XRD curve of the 7×10^{15} He^+ cm^{-2} implanted SiC. The curve shows a main sharp Bragg peak ($\theta = \theta_{Bragg}$) resulting from the unperturbed part of the crystal (bulk SiC) and a diffracted intensity toward the low angle side ($\theta < \theta_{Bragg}$). This latter is ascribed to a dilatation gradient of the lattice along the surface normal direction. A previous study has shown that the

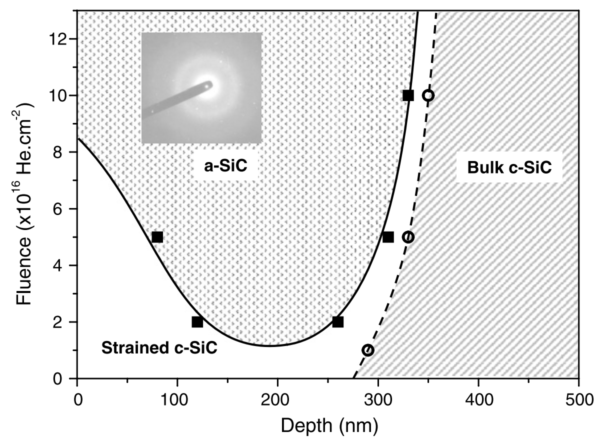

Fig. 1. Schematic 'phase diagram' illustrating the changes in the microstructure of implanted SiC sample as a function of helium fluence (50 keV, *RT*). The thick line plotted from the TEM micrographs represents the amorphous–crystalline transition (a/c). The dotted line that represents the transition between the strained SiC and the bulk, has been deduced both from the strain profile obtained by simulation curves of the XRD curves and from TEM micrographs.

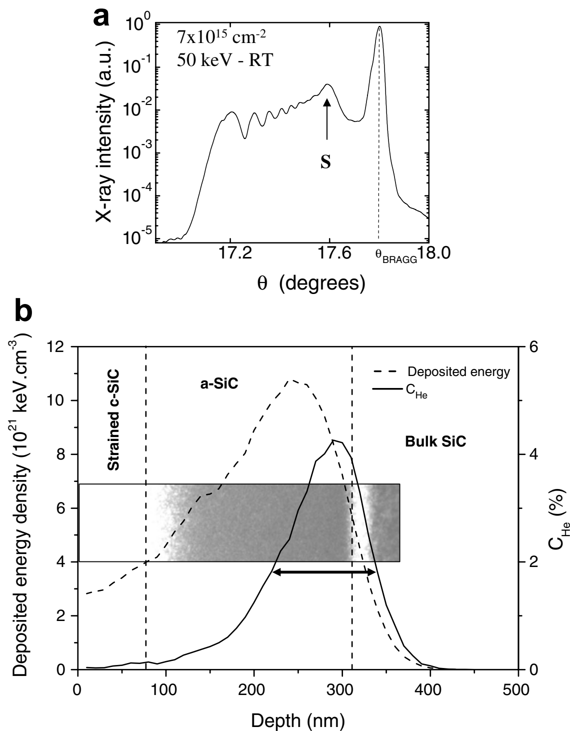

Fig. 2. (a) X-ray scattered intensity distribution along the direction of implantation close to the (0004) Bragg reflection in implanted SiC at $7\times10^{15}\,cm^{-2}$. The satellite peak (S) denotes the near surface-region, and (b) cross-sectional view of the damaged layer of the implanted SiC at 5×10^{16} $He^{+}\,cm^{-2}$. The deposited energy density (dotted line) and ion (continuous line) distributions are also plotted. The arrow denotes the depth's range of observable bubbles.

satellite peak (labelled S on Fig. 2(a)) near θ_{Bragg} comes from the near-surface region [25]. The normal strain $(\Delta d/d)_N(z)$ is found to vary from 1% from the surface up to 4% in the highly damaged zone (furthest part of the curve away from θ_{Bragg}). Both strain values increase with fluence, they reach 1.5 and about 8% respectively at $1\times10^{16}\,cm^{-2}$. The interference fringes result from the coherent diffraction between two zones of same strain on either sides of the maximum damage area. With increasing fluence a continuous amorphous (a-SiC) buried layer is formed (the selected area diffraction pattern clearly shows a halo pattern corresponding to the amorphous phase, see in the inset of Fig. 1) and therefore the normal strain in the highly deposited energy zone can no more be determined. In the near-surface region the normal strain still increases with the fluence, in agreement with the deposited energy [26]. The width of the amorphous layer, determined from TEM micrographs, is plotted in Fig. 1 as a function of the fluence. As an example, the cross-sectional micrograph of the implanted sample at 5×10^{16} $He^{+}\,cm^{-2}$ is presented in Fig. 2(b). The wide damaged layer is made of three different regions. The central layer is an amorphous layer whereas the two side regions are crystalline but exhibit a high density of defects near the amorphous layer (white contrast), not resolvable by conventional TEM. Small bubbles are readily formed in the deeper part of the amorphous region. Ion range and damage calculations have been superimposed on the X-TEM image (Fig. 2(b)). Bubbles do not form on the entire helium depth distribution. This indicates that a buried layer of helium bubbles does not form below some threshold helium concentration, estimated at about 2%. The damage distribution shows that amorphization of silicon carbide occurs for deposited energy of $3–4\times10^{21}\,keV\,cm^{-3}$. Considering these two thresholds, a fluence of $1\times10^{16}\,cm^{-2}$ should avoid both amorphization and bubble formation; only a contrasted zone located near the maximum damage deposition is observed by X-TEM. Increasing the fluence up to $1\times10^{17}\,cm^{-2}$ results in the formation of an amorphous layer extending from the surface to a depth of approximately 340 nm beneath the surface. Bubbles, 1–2 nm in diameter, only form in the implanted layer when the helium concentration exceeds the threshold concentration. The entire part of the implanted crystal being amorphous, there is no more satellite peak on the XRD curve and the diffracted intensity, coming from the transition region at the buried interface, is very low [26].

3.2. Changes in the mechanical properties

Fig. 3 shows the typical load–displacement curves obtained before (a) and after helium implantation at fluences of 7×10^{15} (b), 2×10^{16} (c) and $1\times10^{17}\,cm^{-2}$ (d), correlated with the different microstructures. In unimplanted SiC (a), a pop-in phenomenon, that is an abrupt increase of the penetration depth at a given load, is observed for depths ranging from 60 to 80 nm. This effect has been already reported in SiC [27] and is ascribed in bulk SiC to the first stage of plastic deformation. The deformed volumes are so small that they can be considered as exempt of pre-existing dislocations; the first stage of plastic deformation thus requires homogeneous nucleation of dislocations; the deformation being elastic for lower penetration depths. For implanted SiC (b,c,d), no initial pop-in effect is observed at the beginning of the plastic deformation. The implantation generated defects promote the dislocation nucleation even for very low loads (heterogeneous nucleation of dislocations). However, a pop-in is observed at high fluences (c,d) in the elasto-plastic regime for a penetration depth close to the buried amorphous/crystalline interface. The presence of this pop-in which is the signature of the beginning of the plastic deformation of the bulk SiC substrate, shows that two distinct deformation regimes are involved in the implanted layer and in the bulk SiC substrate.

The hardness values against the penetration depth are plotted in Fig. 4. As seen, in the unimplanted sample (a), the hardness increases with decreasing penetration depth. This Indentation Size Effect (ISE) is often observed in crystalline materials and ascribed to the increasing contribution of geometrically necessary dislocations at small scale [28]. The measured intrinsic hardness (asymptotic value) of bulk

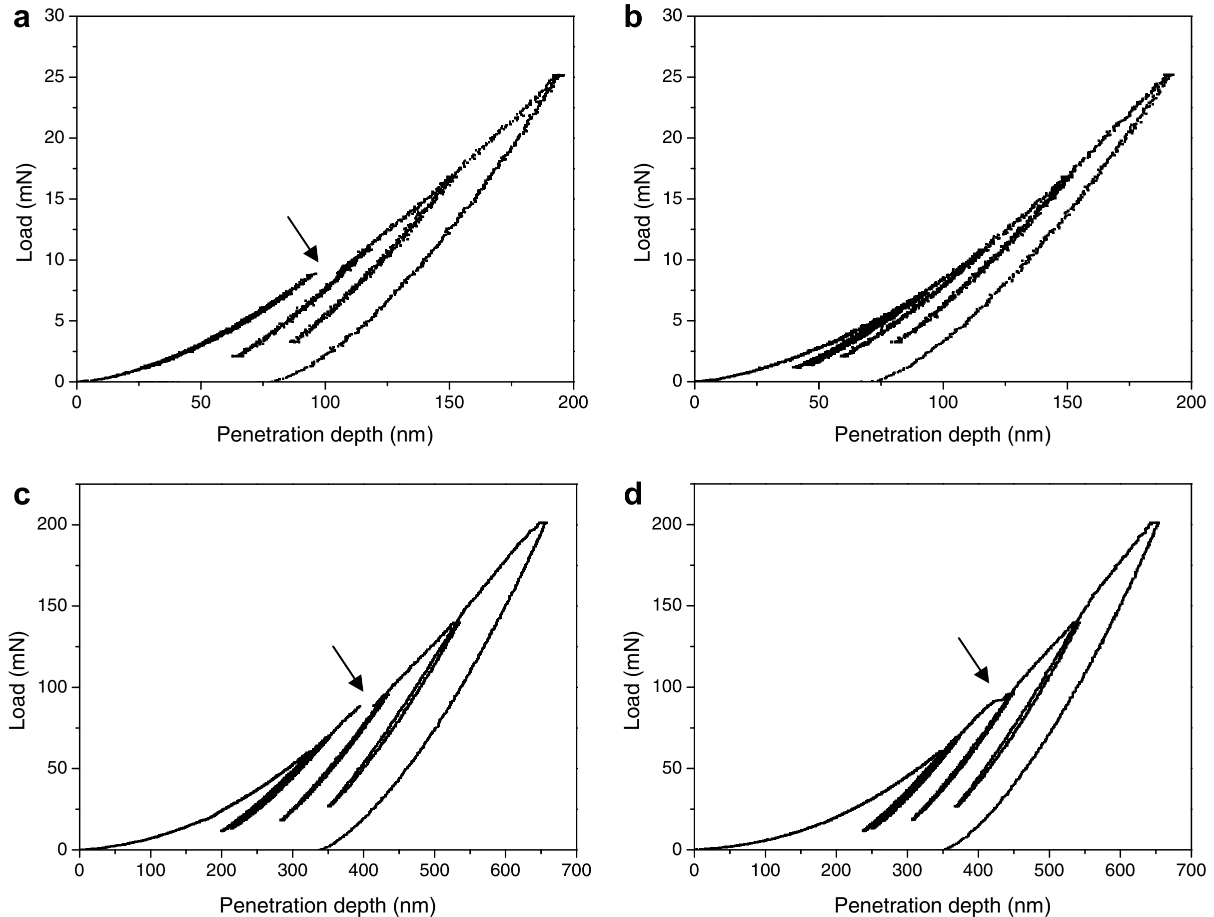

Fig. 3. Typical load–displacement curves performed on unimplanted SiC (a), and helium implanted SiC at different fluences of 7×10^{15} (b), 2×10^{16} (c) and 1×10^{17} cm^{-2} (d). The pop-in events are marked by arrows.

4H–SiC is 37 ± 2 GPa, in good agreement with previous estimates on single crystalline SiC [7]. The elastic reduced modulus is rather constant with the penetration depth and is 510 ± 10 GPa. At low fluence (b), for 7×10^{15} cm^{-2}, no significant changes of hardness values are shown. The point defects or clusters thereof generated all along the ion path induce a normal strain contributing at the ensuing volume change of the implanted region and promote the dislocation nucleation but do not significantly contribute to mechanical changes. For the fluence of 2×10^{16} cm^{-2} (c), the hardness variations against the penetration depth can be divided into three different regions. At low load (stage I) the hardness values are lower than those in bulk SiC and decrease with increasing penetration depth. For penetration depths between 150 and 400 nm approximately (stage II), the hardness increases. Finally, beyond 400 nm (stage III) the hardness drops and levels off at a value slightly under the hardness value of single crystalline SiC (37 ± 2 GPa). These variations will be discussed with regard to AFM observations (see Section 3.3). For the highest fluence (d) where the amorphous state takes place from the as-implanted surface, the hardness values in the near surface region show a decrease of 50%, that is in good agreement with previous experimental results on amorphous SiC [7]. With increasing load the hardness increases to reach a value slightly under the intrinsic value; the substrate effect becoming more and more predominant.

3.3. AFM characterization of indents and discussion

Fig. 5 shows the AFM images of the topography around the nanoindentation imprints. On the unimplanted material (a) the inside of the imprints shows unevenness associated to slip lines due to the emergence of dislocations since it has been previously established that the plastic deformation under high stress of (0001) 6H–SiC is mainly governed by dislocation nucleation and slip [29]. The indent also presents a slight bowing in and radial cracks starting at the corners of the imprint. The bowing in of the imprint is characteristic of a strong elastic recovery of the indentation sides that are pinned by the cracks at the corners. No hillocks are observed, the surrounding surface being flat.

At low fluence, 7×10^{15} cm^{-2} (b), when no amorphization occurs, the mechanical behavior is similar as in implanted SiC (presence of slip lines, same values of hardness). Nevertheless, no radial cracks are observed (b). High compressive stress is induced by implantation as shown by the strain gradient along the vertical axis. The residual

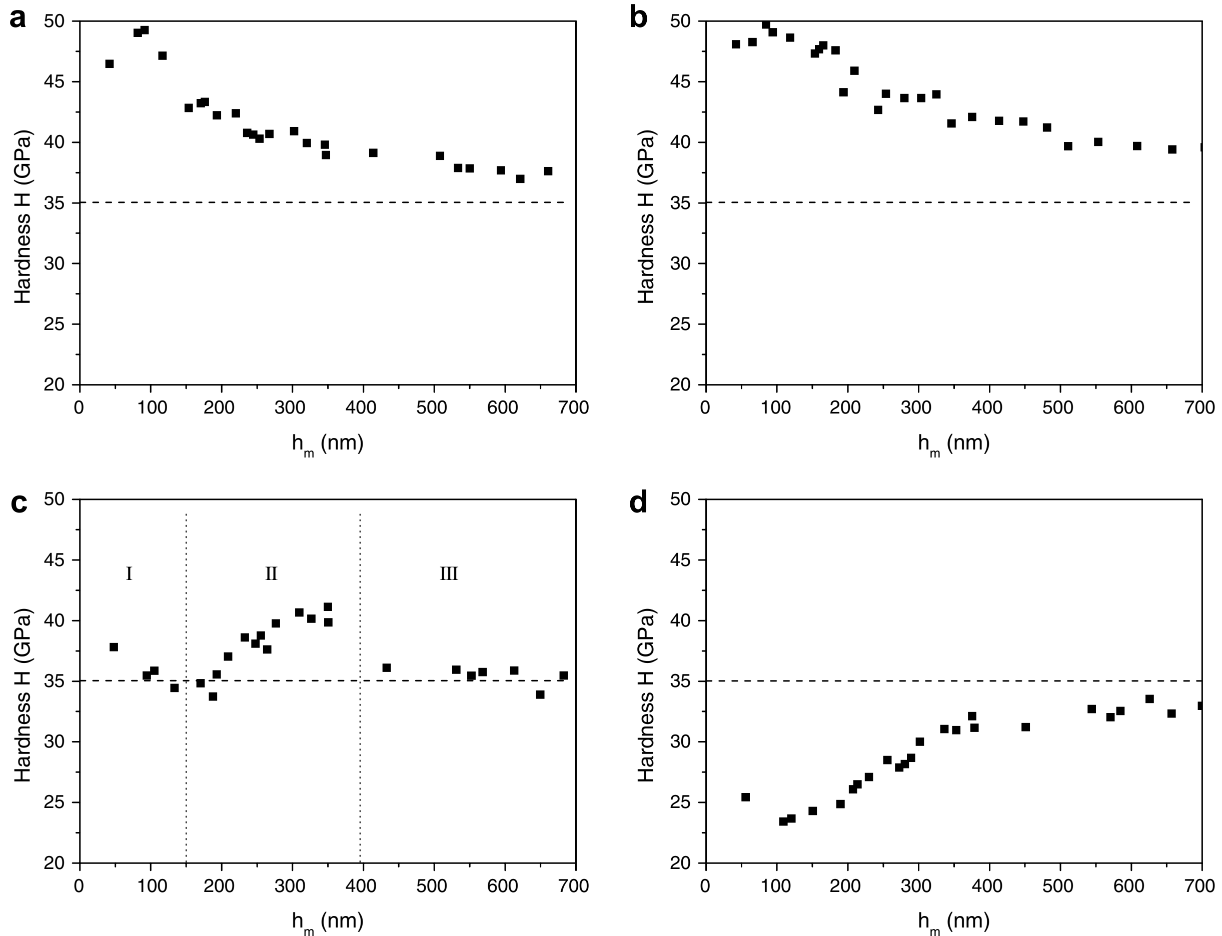

Fig. 4. Hardness versus maximum penetration depth (h_m) curves for unimplanted SiC (a), and helium implanted SiC at different fluences of 7×10^{15} (b), 2×10^{16} (c) and 1×10^{17} cm^{-2} (d).

in-plane stress is thus supposed to impede the crack formation. The as-created defects enhance the dislocation nucleation since no pop-in is observed at the beginning of the plastic deformation.

For the fluence of 1×10^{17} cm^{-2} (d), when all the irradiated volume is in the amorphous state, the indentation imprint reproduces the threefold symmetry of the Berkovich indenter. Unlike the unimplanted material, no slip lines on the inner surfaces of the imprint neither cracks are observed. For lower penetration depths the deformation is solely accommodated by the upper part of the amorphous layer. With increasing penetration depth the crystalline SiC substrate acts as a barrier for the amorphous material flow leading to the formation of hillocks on the surface, Fig. 5(d), and to the hardness increase, Fig. 4(d). At penetration depths above 400 nm the plastic deformation is initiated in the substrate supported by evidence from the pop-in phenomenon and the steady hardness value.

A helium implantation at 2×10^{16} cm^{-2} (c) results into a composite system: strained c-SiC/a-SiC/bulk SiC that leads to a complex hardness/penetration curve with three different stages. In stage I, the hardness is lower than in bulk-SiC. The decrease of the hardness with increasing penetration is due to both the ISE in the upper c-SiC layer and the increasing solicitation of the softer buried amorphous layer (a-SiC). In stage II, the hardness values raise and large hillocks appear around the indent (white spots on the inset of Fig. 5(c)). Close examination of the imprint shows some slip lines but only in the deeper part of the residual imprint, the shallower part being unsheared. This observation shows that for very low load penetration depths (stage I) the deformation is accommodated by the implanted c-SiC (dislocation plasticity). For higher penetration depths the plastic deformation mainly takes place in the a-SiC layer, the deformation in the upper c-SiC layer being elastic (membrane effect). The a-SiC layer attempts to elastically flex and bends the c-SiC layer which, in turn, resists and constrains the upward movement of displaced a-SiC material, thus increasing its hardness. This effect is drawn on Fig. 6 after indenter tip removal. This ‘constraining coating’ effect has been previously explained by McGurk and Page [30] in case of hard coating on ductile substrate. To confirm the coating effect and to determine the critical depth at which the amorphous state is fully solicited, the volumes of the emerging hillocks (V_h) and of the residual

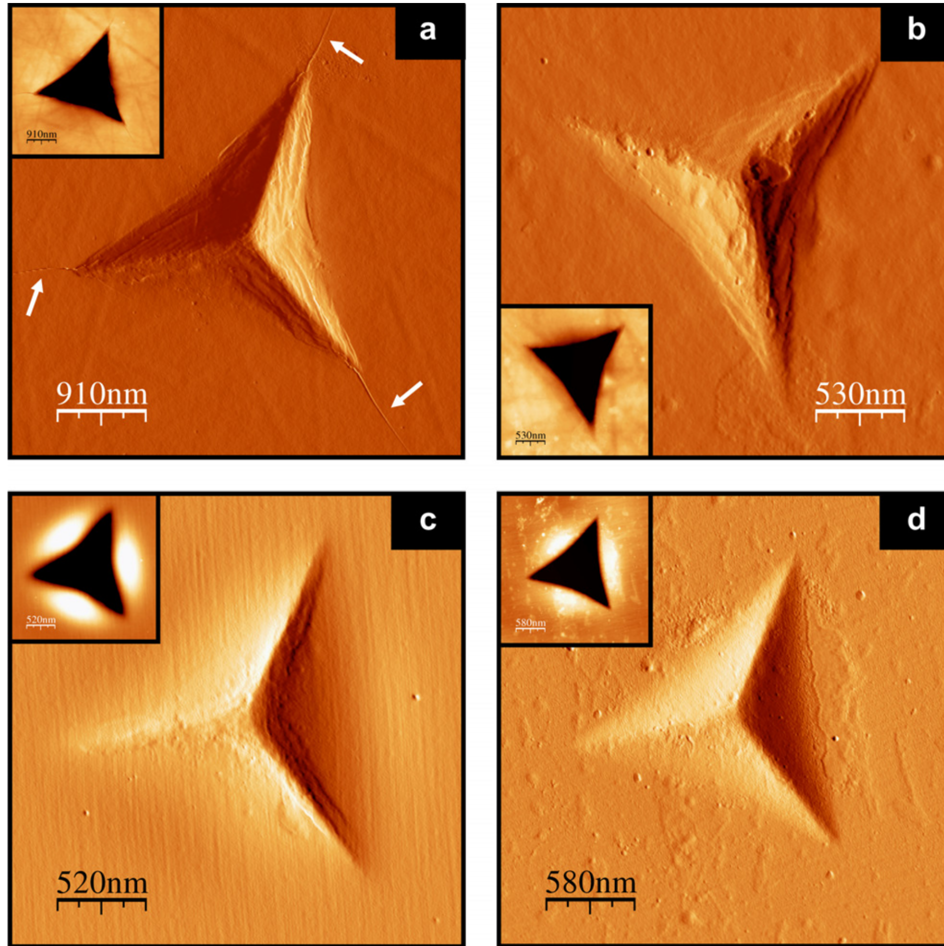

Fig. 5. Tapping mode AFM images (error signal mode) of nanoindentation imprints in unimplanted SiC (a) and helium implanted SiC at different fluences of 7×10^{15} (b), 2×10^{16} (c) and 1×10^{17} cm^{-2} (d). The insets present the corresponding topography images. Cracks on the corner of the imprint are only observed in unimplanted SiC (see arrows in (a)).

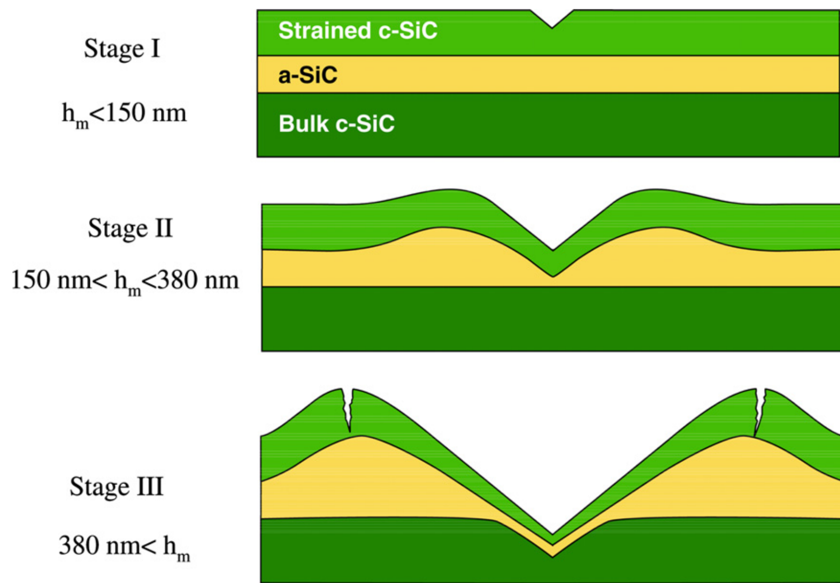

Fig. 6. Drawing of the confining effect induced by the upper strained c-SiC layer during nanoindentation of the 2×10^{16} He^+ cm^{-2} implanted SiC where a buried amorphous layer is formed (a-SiC) on a crystalline substrate (bulk SiC). In stage I, the plastic deformation takes place in the upper crystalline SiC layer. In stage II, the deformation is accommodated by the buried amorphous layer and results in hillock formation. In stage III, plastic deformation takes place in the crystalline substrate. For high penetration depth, the confining effect is also overcome by cracks in the upper c-SiC layer in the hillocks region.

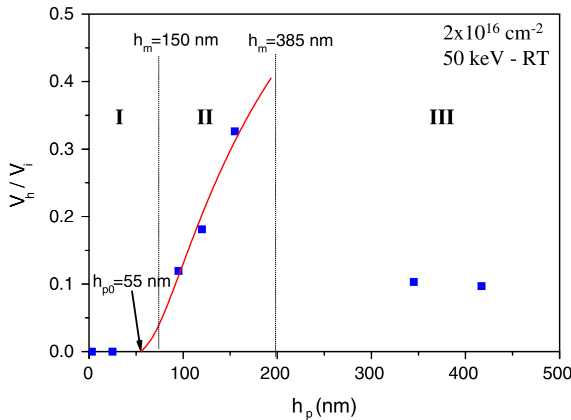

Fig. 7. Ratio of the hillock volume, V_h, over the residual imprint volume, V_i, as a function of the residual penetration depth h_p for the 2×10^{16} He^+ cm^{-2} implanted SiC. In stage II, the volume of the hillocks corresponds to the volume of the matter displaced below the critical depth $h_{p0} = 55$ nm ($h_m = 100$ nm). The value of h_{p0} has been determined using a fitting function of the V_h/V_i ratio (continuous line).

imprints (V_i) have been determined by AFM. The ratio V_h/V_i versus the residual penetration depth h_p is plotted on Fig. 7. As for the hardness curve three stages are observed. In stage I that is at low penetration depth no hillocks are formed ($V_h = 0$). In stage II, the ratio of volumes strongly increases with penetration depth. In stage III, the ratio falls down due to the activation of plastic deformation in bulk SiC. The V_h/V_i values have been fitted by using the following function:

$$\frac{V_h}{V_i}(h_p) = \frac{V(h_p - h_{p0})}{V(h_p)},$$

where $V(h_p)$ is the volume of an imprint of residual depth h_p calculated from the calibrated shape of the Berkovich indenter used in this study and h_{p0} the residual penetration depth from which hillocks appear on the surface; $V(h_p - h_{p0})$ is thus the partial volume of the imprint lying below h_{p0}. This function fits well the experimental data's and gives a critical value of the residual depth $h_{p0} = 55$ nm that corresponds to a maximum penetration depth under loading, h_m, of about 100 nm. This latter value is close to the transition value from stage I to stage II on the hardness curve, Fig. 4(c), and shows that the 'constraining coating' effect is observed for penetration depths in front of the strained/amorphous interface. The partial volume of the imprint, $V(h_p - h_{p0})$, lying between the bottom of the indent h_p and h_{p0}, corresponds to the hillocks volumes. This clearly shows that the hillocks result from the flowing of amorphous SiC induced by indentation. A large pop-in effect characteristic of the incipient plasticity in the substrate is observed on loading curves for maximum penetration depths of about 400 nm, i.e., when the indenter penetrates into the substrate. That leads to a drop of the hardness value (stage III) showing that the substrate undergoes the deformation overcoming thus the 'constraining coating' effect. For maximum penetration depths, h_m, of about 600 nm, AFM observations show the bulging and cracking of the strained c-SiC upper layer. Eventually, the displaced volume of a-SiC becomes too high to be still constrained by the upper layer which buckles and cracks.

4. Conclusion

The effects of room temperature helium implantation at high fluence on the surface mechanical properties and microstructure of 4H–SiC have been investigated. The near-surface nanohardness has been found to be dependent on the helium fluence when exceeds 1×10^{16} cm^{-2} and tends to decrease with increasing fluence. Nevertheless at lower fluences the implantation induces a vertical strain gradient, suppresses the crack formation and enhances the dislocation generation avoiding the pop-in effect. With increasing fluence, a buried amorphous layer is formed as well around the maximum of the deposited energy density. The hardness-depth curve shows different stages explained by a 'constraining coating' effect. It is shown that the appearance of hillocks on the surface is directly related to the solicitation of the amorphous layer. In particular, a one-to-one proportionality between the volumes of hillocks with the volume of the indenter in the amorphous layer has been observed. At 1×10^{17} cm^{-2}, the entire part of the implanted crystal is amorphous and a decrease of about 50% in the hardness value is observed. This study clearly shows that damage created by helium implantation induce a degradation of the mechanical properties of 4H–SiC and that for intermediate fluences a composite system forms as well leading to complexes deformation processes that need specific studies.

References

[1] L.L. Snead, R.H. Jones, A. Kohyama, P. Fenici, J. Nucl. Mater. 233–237 (1996) 126.

[2] S. Ueda, S. Nishio, Y. Seki, R. Kurihara, J. Adachi, S. Yamazaki, DREAM Design Team, J. Nucl. Mater. 258–263 (1998) 1589.

[3] R.H. Jones, L. Giancarli, A. Hasegawa, Y. Katoh, A. Kohyama, B. Riccardi, L.L. Snead, W.J. Weber, J. Nucl. Mater. 307–311 (2002) 1057.

[4] E.E. Bloom, S.J. Zinkle, F.W. Wiffen, J. Nucl. Mater. 329–333 (2004) 12.

[5] E. Wendler, A. Heft, W. Wesch, Nucl. Instrum. and Meth. B 141 (1998) 105.

[6] L.L. Snead, S.J. Zinkle, J.C. Hay, M.C. Osborne, Nucl. Instrum. and Meth. B 141 (1998) 123.

[7] L.L. Snead, J.C. Hay, J. Nucl. Mater. 273 (1999) 213.

[8] S. Nogami, A. Hasegawa, L.L. Snead, J. Nucl. Mater. 307–311 (2002) 307.

[9] C.J. McHargue, J.M. Williams, Nucl. Instrum. and Meth. B 80–81 (1993) 889.

[10] W.J. Weber, L.M. Wang, N. Yu, N.J. Hess, Mater. Sci. Eng. A 253 (1998) 62.

[11] A. Hasegawa, M. Saito, S. Nogami, K. Abe, R.H. Jones, H. Takahaski, J. Nucl. Mater. 264 (1999) 335.

[12] A. Hasegawa, S. Nogami, T. Aizawa, K. Katou, K. Abe, J. Nucl. Mater. 307–311 (2002) 1152.

[13] T. Taguchi, N. Igawa, S. Miwa, E. Wakai, S. Jitsukawa, L.L. Snead, A. Hasegawa, J. Nucl. Mater. 335 (2004) 508.

[14] S. Nogami, A. Hasegawa, L.L. Snead, R.H. Jones, K. Abe, J. Nucl. Mater. 329–333 (2004) 577.
[15] J. Chen, P. Jung, H. Ullmaier, J. Nucl. Mater. 336 (2005) 194.
[16] A.J. Frias Rebelo, H.W. Scholz, H. Kolbe, G.P. Tartaglia, P. Feneci, J. Nucl. Mater. 258–263 (1998) 1582.
[17] L.L. Snead, R. Scholz, A. Hasegawa, A. Frias Rebelo, J. Nucl. Mater. 307–311 (2004) 1141.
[18] T. Suzuki, T. Yano, T. Mori, H. Miyazaki, I. Iseki, Fus. Technol. 27 (1995) 314.
[19] J.F. Ziegler, J.P. Biersack, U. Littmark, The Stopping and Range of Ions in Solids, <http://www.srim.org>.
[20] G. Lucas, L. Pizzagalli, Phys. Rev. B 72 (2005) 161202.
[21] C.H. Zhang, S.E. Donnelly, V.M. Vishnyakov, J.H. Evans, J. Appl. Phys. 94 (2003) 6017.
[22] A.C. Fischer-Cripps, Surf. Coat. Technol. 200 (2006) 4153.
[23] J. Woirgard, J.-C. Dargenton, J. Mater. Res. 12 (1997) 2455.
[24] I. Horcas, R. Fernandez, J.M. Gomez-Rodriguez, J. Colchero, J. Gomez-Herrero, A.M. Baro, Rev. Sci. Instrum. 78 (2007) 013705.
[25] A. Declémy, E. Oliviero, M.F. Beaufort, J.F. Barbot, M.L. David, C. Blanchard, Y. Tessier, E. Ntsoenzok, Nucl. Instum. and Meth. B 186 (2002) 318.
[26] S. Leclerc, A. Declémy, M.F. Beaufort, C. Tromas, J.F. Barbot, J. Appl. Phys. 98 (2005) 113506.
[27] T.F. Page, W.C. Oliver, C.J. McHargue, J. Mater. Res. 7 (1992) 450.
[28] F. Gao, W.J. Weber, Phys. Rev. B 69 (2004) 224108.
[29] T.F. Page, G.M. Pharr, J.C. Hay, W.C. Oliver, B.N. Lucas, E. Herbert, L. Riesler, Mater Res. Soc. Symp. Proc. 522 (1998) 53.
[30] M.R. McGurk, T.F. Page, Surf. Coat. Technol. 92 (1997) 87.